nature communications



Article

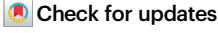
https://doi.org/10.1038/s41467-025-64240-1

Injectable micropore-forming microgel scaffold for neural progenitor cells transplantation and vascularization after stroke

Received: 27 January 2025

Accepted: 11 September 2025

Published online: 23 October 2025



Huayan Wu^{1,5}, Ze Liu^{2,5}, Zijie Zhang^{1,5}, Zhongqing Liu², Zhiqiang Gao¹, Muyassar Mamtilahun $^{\circ}$ ², Huanhong Li², Yaoyao Li², Shengju Wu², Guosheng Tang $^{\circ}$ ³, Guo-Yuan Yang², Wanlu Li $^{\circ}$ ² \boxtimes , Shaorong Gao $^{\circ}$ ⁴ \boxtimes & Mian Wang $^{\circ}$ ¹ \boxtimes

Stem cell therapy for stroke is hindered by poor cell survival and integration within the ischemic microenvironment. Injectable microgels have been widely employed in cell delivery for their ability to promote cell infiltration, but dense hydrogel networks often limit cell survival. Here we present an injectable microgel-matrix composite scaffold that combines microporous microgels for neural progenitor cells (NPCs) delivery with interstitial spaces to support vascular growth. Using a gas-shearing fabrication approach, primary rat NPCs are efficiently encapsulated in phase-separated microporous microgel (PSMM), exhibiting superior survival and proliferation. In vitro studies demonstrate that PSMM scaffolds support endothelial cell (EC) sprouting and vascular formation, and in ischemic stroke rats, this formulation significantly enhance NPC loading capacity, survival, and differentiation, along with increased EC proliferation and infiltration. Ultimately, the microgel-matrix scaffold enhances long-term neurological recovery in stroke models, offering an efficient strategy that couples high cell loading with vascularization to advance regenerative medicine.

Stroke is a leading cause of death and disability globally. As a most common type of stroke, ischemic stroke occurs when cerebral blood vessels are transiently or permanently occluded, reducing the flow of oxygen to the brain, leading to neuronal death, inflammation, and persistent neurological impairments^{1,2}. Currently, revascularization

strategies for ischemic stroke are limited to FDA-approved tissue plasminogen activator (tPA) and endovascular thrombectomy. However, tPA is constrained by a narrow 4.5-h treatment window and a high risk of hemorrhagic transformation, while thrombectomy, though effective, is invasive and dependent on advanced surgical expertise

¹State Key Laboratory of Cardiology and Medical Innovation Center, Institute for Regenerative Medicine, Shanghai East Hospital, Frontier Science Center for Stem Cell Research, School of Life Sciences and Technology, Tongji University, Shanghai, China. ²School of Biomedical Engineering, Shanghai Jiao Tong University, Shanghai, China. ³Guangzhou Municipal and Guangdong Provincial Key Laboratory of Molecular Target and Clinical Pharmacology, the NMPA and State Key Laboratory of Respiratory Disease, School of Pharmaceutical Sciences and the Fifth Affiliated Hospital, Guangzhou Medical University, Guangzhou, China. ⁴Shanghai Key Laboratory of Maternal Fetal Medicine, Clinical and Translational Research Center of Shanghai First Maternity and Infant Hospital, Shanghai Institute of Maternal-Fetal Medicine and Gynecologic Oncology, Frontier Science Center for Stem Cell Research, School of Life Sciences and Technology, Tongji University, Shanghai, China. ⁵These authors contributed equally: Huayan Wu, Ze Liu, Zijie Zhang.

and equipment³. These limitations underscore the pressing need for alternative therapeutic approaches that are safer, less time-restricted, and capable of enhancing neurological recovery.

Stem cell therapy has gained increasing attention for its potential to promote post-stroke outcomes⁴. Among various candidates, neural progenitor cells (NPCs) are particularly promising due to their ability to differentiate into neurons, astrocytes, and oligodendrocytes, offering potential for neuronal replacement in damaged brain regions⁵. Early-phase clinical trials since 2005 have explored the safety of NPC transplantation using intravenous, intraventricular, or intracerebral routes⁶⁻⁸. However, most of these studies remain limited to Phase 1 or 2 with small patient cohorts, and conclusive evidence on therapeutic efficacy is still lacking. This highlights the need for more robust preclinical data to guide clinical translation. Preclinical studies have illuminated that transplantation of NPCs reduced brain infarction and promoted neurological function recovery by secreting protective factors to modulate neuroinflammation, enhancing angiogenesis, and stimulating endogenous neurogenesis9. However, it remains challenging to translate these findings to clinical practice because transplanted NPCs are poor at homing, surviving, and integrating in the ischemic microenvironment^{10,11}.

Localized delivery of stem cells along with biomaterials enables addressing these challenges by offering suitable biophysical and biochemical cues to better regulating cell function in vivo¹². Injectable hydrogels, such as hyaluronic acid13 and self-assembling peptides14, have been shown to support NPC survival, modulate the inflammatory niche, and promote angiogenesis. However, their mechanical fragility and limited vascular integration often result in suboptimal long-term outcomes. For instance, hyaluronic acid-based hydrogel improved the survival of NPCs in ischemic stroke mice, though they failed to sustain cell survival beyond 7 days post-transplantation¹³. Alternative platforms such as poly (lactic-co-glycolic acid)-based microparticles have also been explored to deliver NPCs, showing short-term integration and survival. However, the absence of vascularization, which is crucial for delivering nutrients to the transplanted NPCs, hindered their longterm survival and differentiation¹⁵. More recently, conductive scaffolds have been proposed to enhance neuronal differentiation through electrical stimulation, but their translation remains at an early preclinical stage¹⁶.

Microgel scaffold, composed of packed hydrogel microparticles, represent a novel class of biomaterials with advantages such as injectability, defined physicochemical properties, and flexibility in engineering microparticle components¹⁷⁻¹⁹. Their inherent interconnected porosity facilitates cellular infiltration and tissue remodeling²⁰. A recent study showed that injection of hyaluronic acidbased microgel scaffolds into the stroke cavity reduced brain atrophy and preserved axons in mice. Reparative astrocytes were observed within the micropores and infiltrated the lesion area, coinciding with axonal penetration into the lesion²¹. In addition to serving as structural supporters, microgels have also been utilized as carriers for stem cell delivery during tissue regeneration²²⁻²⁴. However, previous studies reported low cell-loading efficiency, with most stem cells adhering to the surface or becoming encapsulated within microgels lacking sufficient internal space to support cell survival and proliferation. To overcome this limitation, we develop a micropore-forming, cell-laden hydrogel based on an aqueous two-phase system (ATPS), which significantly enhances cell viability, proliferation, and spreading compared to conventional nanoporous constructs^{25,26}. We therefore hypothesize that incorporating this phase-separation strategy into conventional microgels could optimize their internal architecture, providing more supportive microenvironment transplanted NPCs.

In this study, we develop a microgel-matrix composite scaffold comprising dual-features, such as intrinsic microporosity within microgels and interstitial space between microgels filled with a supportive matrix for delivering NPCs into the ischemic stroke cavity and investigate their neurogenesis and vascular integration (Fig. 1). The microporous microgels (MM) are fabricated using an oil-free gasshearing strategy, incorporating a cell-laden, pore-forming alginate/polyvinyl alcohol (PVA) system to create internal microscale porosity. These microgels are then packed within a Matrigel/collagen I (M/C) matrix, forming the interstitial phase that supports angiogenesis. We systematically assess the porosity, injectability, and post-injection viability of NPCs within this microgel-matrix system in comparison to traditional non-composite bulk microgels. Finally, NPC-loaded microgel-matrix scaffolds are transplanted into the ischemic cavity of rats 7 days after injury, supporting NPC survival, infiltration, and differentiation, while also enabling the infiltration of host endothelial cells (ECs) and promotion of vascular formation.

Results

Fabrication and characterization of the phase-separated microporous microgel (PSMM) scaffold

We first prepared micropore-forming hydrogels with micro-sized voids using an ATPS approach²⁵⁻²⁷. Previously, we demonstrated the production of such hydrogels using gelatin methacryloyl (GelMA) and either dextran or PVA emulsions, which were suitable for light-assisted curing applications²⁵. In this study, to adapt the phase-separated hydrogel for microgel fabrication, we used the same PVA as a sacrificial material to create voids, but replaced GelMA with alginate (Fig. 2A). Alginate, as a natural anionic polysaccharide derived from brown seaweed, forms hydrogel networks via ionic crosslinking between its guluronate blocks and divalent cations (Ca²⁺) through the "egg-box" model (Supplementary Fig. 1)²⁸. To control the size of the generated micropores, we maintained a fixed concentration of 0.75 wt.% alginate while modulating the PVA concentrations to 3, 4, and 5 wt.%, resulting in a narrow distribution of $48.69 \pm 20.27 \,\mu m$ at the concentration of 5 wt.% PVA. The stability of the pore-forming hydrogel was evaluated, revealing that higher PVA concentrations in the ATPS, whether freshly prepared or stored for several hours at room temperature, consistently kept closed porosity (Supplementary Fig. 2). In contrast, formulations with lower PVA concentrations showed significantly reduced performance after prolonged storage due to marked phaseseparation. Imaging of fluorescein isothiocyanate (FITC)-labeled alginate confirmed that micropores were evenly distributed in the 0.75 wt.% alginate/5 wt.% PVA formulation (Fig. 2B), which was used in subsequent experiments.

Next, a gas-shearing method was employed to fabricate microgels. The spray ejector device consisted of a central needle (for the alginate/PVA solution) and an outer needle (air flow, Fig. 2B and Supplementary Fig. 3A). Through the space between the inner and outer needles, nitrogen gas generated shear forces that enabled the formation of microgels. Notably, microgels were successfully produced in an ultrahigh-throughput process (8123.50 ± 488.35 particles min⁻¹, Fig. 2C) with tight control over microgel size compared to traditional microfluidic method (310.50 ± 32.97 particles min⁻¹, Fig. 2C and Supplementary Fig. 3B). We further detected the removal of PVA from microgels. Fluorescence imaging revealed its homogeneous distribution within the alginate network and a gradual signal decline over time, becoming nearly undetectable at 24 h (Fig. 2D and Supplementary Fig. 4). To quantify this process, rhodamine B absorbance at 562 nm is suitable for detecting rhodamine B-labeled PVA release²⁹. Accordingly, spectrophotometric analysis of the supernatant showed a timedependent increase in absorbance at 562 nm, confirming progressive release. After complete PVA release, fluorescence imaging revealed a porous morphology in PSMM, in contrast to the homogeneous structure observed in MM (Fig. 2E). By adjusting the rates of the air flow, we modulated the diameters of the resulting microgels. As shown in

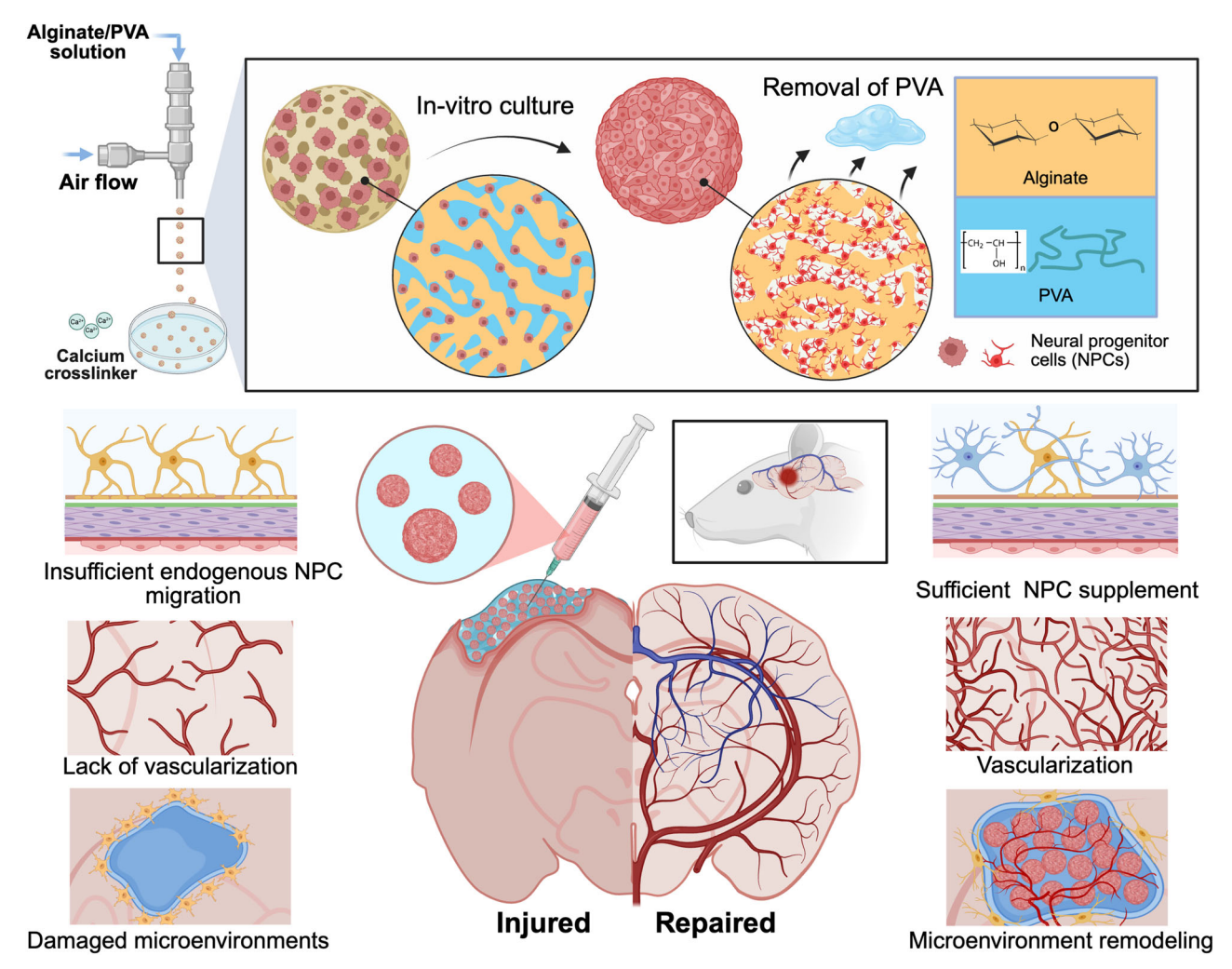


Fig. 1 | **Schematic representation of PSMM fabrication for encapsulating NPCs and the in vivo application in ischemic stroke rats.** The PSMM was prepared using gas-shearing method with an alginate/PVA solution. This engineered PSMM microgel-matrix composite combined two essential features: a microporous microgel core to promote stem cell proliferation and an interstitial matrix to support endothelial cell migration and vascular development. Primary rat NPCs were

encapsulated within PSMM, demonstrating improved survival and rapid proliferation. During brain tissue repair, the injectable PSMM scaffold allowed sufficient NPC supplement, enhanced survival and differentiation of transplanted NPCs, along with accelerated vascularization. Source data are provided as a Source Data file. Schematic created in BioRender. Wang, M. (2025), https://BioRender.com/4h45396.

Supplementary Fig. 5, FITC-labeled alginate microgels with diameters of 249.98 \pm 4.69, 346.13 \pm 10.67, 437.07 \pm 16.60 μ m were fabricated using high, medium, and low flow rates, respectively.

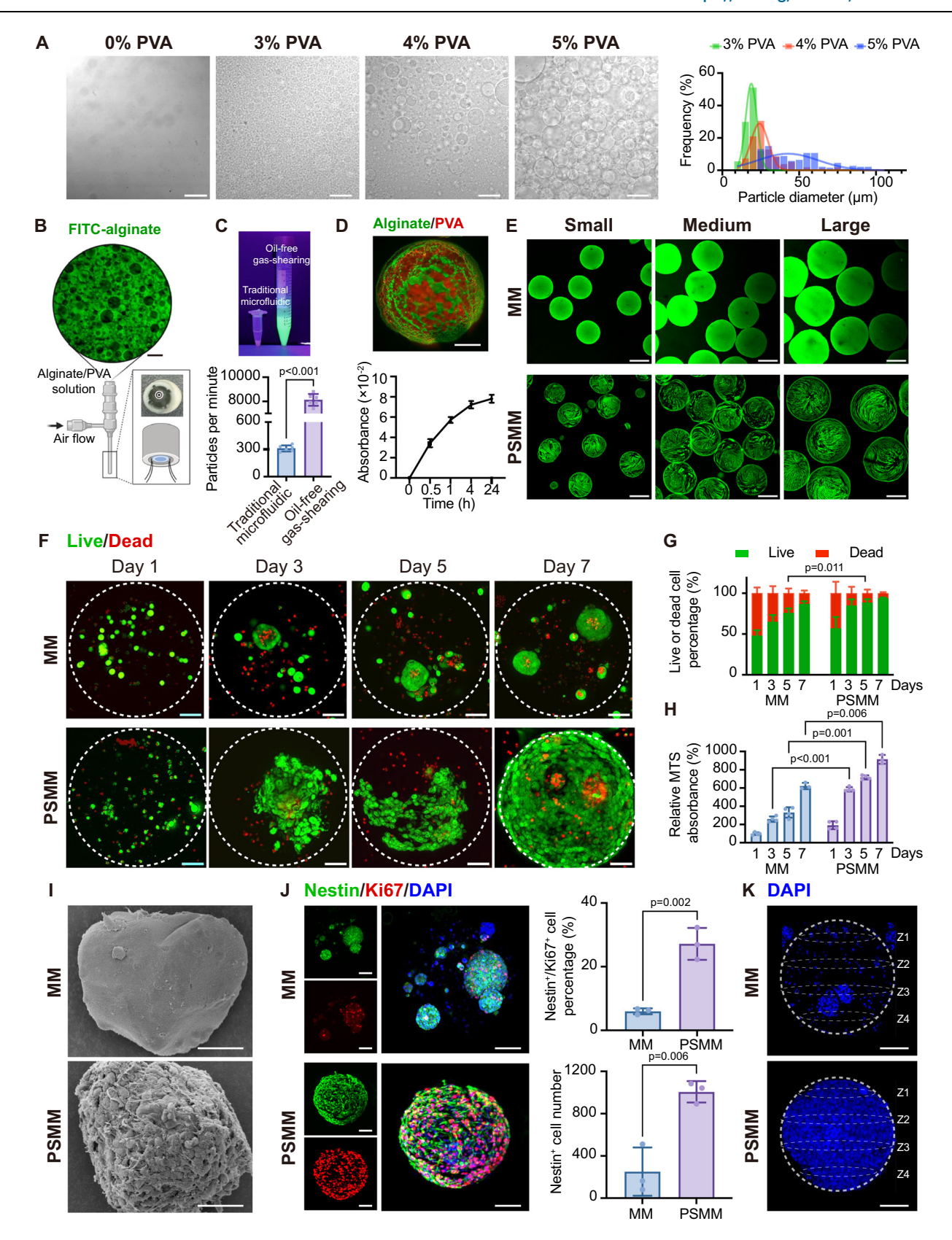
PSMM scaffold preserves the long-term survival of NPCs in vitro

Our hypothesis was that conventional bulk hydrogel microgels could be improved with a micropore-forming strategy, providing encapsulated NPCs with a more cell-friendly microenvironment. To test this, primary NPCs isolated from rats (Supplementary Fig. 6) were mixed with either an alginate or alginate/PVA solution to produce microgels with either nano-sized or micro-sized pores. After 1 day of culture, no significant difference was observed in live/dead cell percentage between nano-sized and micro-sized porous microgels (Fig. 2F, G). However, cell viability in PSMM increased to 84.71 ± 7.82% after 3-days culture, compared to lower viability observed in MM ($64.62 \pm 8.63\%$). By Day 7 of NPC culture, only a few dead cells were observed in PSMM. Meanwhile, the cell metabolic activity detected by the 3-(4,5-dimethylthiazol-2-yl)-5-(3-carboxymethoxyphenyl)-2-(4-sulfophenyl)-2Htetrazolium (MTS) assay was increased with the culture time both in MM and PSMM, but a higher level was presented in the PSMM group (Fig. 2H). NPCs in PSMM maintained significantly higher metabolic activity 7 days of culture.

The cell morphology on both the surface and interior of microgels was visualized by scanning electron microscope (SEM) images (Fig. 21). Intentional fracturing of NPC-laden PSMM revealed the uniform distribution of proliferated NPCs throughout the porous interior, consistent with the observed proliferation results (Supplementary Fig. 7). NPC proliferation was further assessed with immunostaining of NPC marker (Nestin) and proliferation marker (Ki67) at 7 days after culture, showing a higher Nestin⁺/Ki67⁺ cell percentage in the PSMM group compared to the MM counterpart (Fig. 2J). The three-dimensional (3D) DAPI imaging confirmed not only increased cell density but also improved spatial distribution in the PSMM group (Fig. 2K and Supplementary Fig. 8). Quantitative analysis revealed an 8.67-fold increase in cell number and significantly more uniform distribution in PSMM relative to MM. Thus, PSMM facilitated the survival and proliferation of NPCs up to 7 days in vitro, resulting in a dramatically enhanced cell loading capacity compared to bulk alginate microgel.

Microgel-matrix composite facilitates injectability and biocompatibility

Microgel scaffolds, due to their inherent porous structure, have been shown to promote enhanced cell infiltration and angiogenesis compared to bulk hydrogels³⁰. To visualize the porosity of microgel



scaffolds in the absence of M/C matrix, microgels were packed with FITC-dextran and observed using confocal microscopy. 3D renderings, generated with IMARIS software, revealed that aggregated microgels exhibited distinct characteristics depending on their particle microstructures (Fig. 3A). The pore size distribution results showed no significant differences for pores close to the size of the microgels

(Fig. 3B). However, a clear statistical difference was observed for smaller pores, indicating that the internal microstructure influences the overall pore distribution without the hydrogel. Upon incorporation of the M/C matrix, the original void spaces between microgels were occupied by the interstitial matrix (Fig. 3C). The overall porosity in absence of M/C matrix varied independently of microgel

Fig. 2 | **Fabrication and characterization of PSMM scaffolds, and improved NPC survival in vitro.** A Optical images of alginate/PVA emulsions with different PVA concentrations and corresponding size distributions. **B** Schematic of the gasshearing method, with a 5 wt.%-PVA emulsion construct insert. Schematic created in BioRender. Wang, M. (2025), https://BioRender.com/vbm9qww. **C** Comparison of microgels fabricated using oil-free gas-shearing and traditional microfluidic methods, with quantitative production rates. **D** Fluorescence image showing alginate (green) and PVA (red) distribution immediately after fabrication. Quantification of PVA release at 562 nm in the supernatant. **E** Fluorescence micrographs of MM and PSMM prepared at varied flow rates. Experiment was independently repeated three times with similar results. **F** Live/dead staining of NPCs cultured in MM and PSMM on Days 1, 3, 5, and 7. The dashed line represents microgel boundary. Experiment was independently repeated three times with similar results. **G** Quantitative of live/dead cell percentages from (**F**). **H** NPC metabolic activity by

MTS assay. I SEM images showing MM and PSMM scaffold structures and encapsulated NPCs on Day 7. Experiment was independently repeated three times with similar results. J Fluorescence micrographs of Nestin (green) and Ki67 (red) of NPCs on Day 7 with quantification. **K** 3D reconstructed DAPI (blue) images of NPCs in MM and PSMM on Day 7. The dashed line represents microgel boundary. Experiment was independently repeated three times with similar results. Scale bars, **A**, **B**, 100 μ ; **D**, **F**, **J** and **K**, 50 μ ; **E**, 200 μ ; **I**, 25 μ m. Data are mean values \pm SDs. **C**, n = 6 technically independent samples, unpaired t test; **D**, n = 3 technically independent samples for the data of Days 1, 3, and 5; n = 3 technically independent samples for the data of Day 7, two-way ANOVA; **J**, n = 3 technically independent samples, unpaired t test. Source data are provided as a Source Data file.

microstructure, rising from $19.80\pm0.96\%$ in MM to $47.78\pm3.76\%$ in PSMM (Fig. 3D). Interestingly, the interstitial space was comparable with porosity after mixing with M/C matrix, indicating the void spaces were fully occupied by matrix.

While alginate-based microgels possess advantages such as high throughput production and fast crosslinking, they exhibit poor cohesion and mechanical instability when subjected to shear stress during injection. This shear stress not only disrupted microgel integration but also significantly impaired the viability of encapsulated NPCs (Fig. 3E and Supplementary Fig. 9). To address these limitations, we introduced a M/C matrix to generate the PSMM scaffold, which effectively preserved cell viability during injection and enhanced the mechanical integrity of the microgel construct. As shown in Supplementary Fig. 10A, B and Supplementary Movie 1, the addition of M/C significantly improved the injectability and mechanical integrity of the microgel scaffolds. This strategy is consistent with previous studies demonstrating that hybridizing microgels with an interstitial phase enhances injectability and mechanical robustness³¹⁻³³. Notably, both cell-laden and cell-free microgel-matrix formulations produced continuous filaments upon syringe extrusion, with comparable filament lengths under identical injection rates and durations (Supplementary Fig. 10A, B and Supplementary Movie 1). This indicates that encapsulation of NPCs did not adversely affect injectability. In contrast, microgels lacking the M/C matrix exhibited discontinuous and significantly shorter extrudates regardless of cell loading, underscoring the critical role of the interstitial matrix in maintaining extrusion continuity and mechanical cohesion. The injectability of the PSMM scaffold was also validated by loading the hydrogel into a syringe and stereotaxically injecting it into the stroke cavity of rat. The hydrogel was continuously delivered, maintaining its structural integrity with intact and packed microgels (Supplementary Fig. 10C).

We further evaluated the rheological behaviors of microgel scaffolds by conducting oscillatory rheometry to compare the modulus and viscosity of MM and PSMM formulations. The microgel-based hydrogel developed in this study exhibited rheological properties that are crucial for injectability. The results demonstrated that the microgel samples exhibited superior shear-thinning characteristics, as their viscosity decreased as shear rate increased (Fig. 3F). Additionally, microgel samples showed notably higher storage moduli compared to the bulk control, likely due to friction or interlocking between microparticles and the hydrogel under shear stress (Fig. 3G). Under high strain conditions, microgel samples experience yielding, enabling them to flow through confined spaces of syringe needles (G'' > G'). When subjected to cyclic regimens alternating between high (500%) and low (1%) strain, all samples in this study demonstrated shearthinning and self-healing characteristics (Fig. 3H). Additionally, the mechanical properties of all samples were fully restored once the high strain was removed. Accordingly, our results highlight variations in rheological behavior influenced by differences in particle porosity and emphasize the clinical significance of injectability for minimally invasive delivery applications.

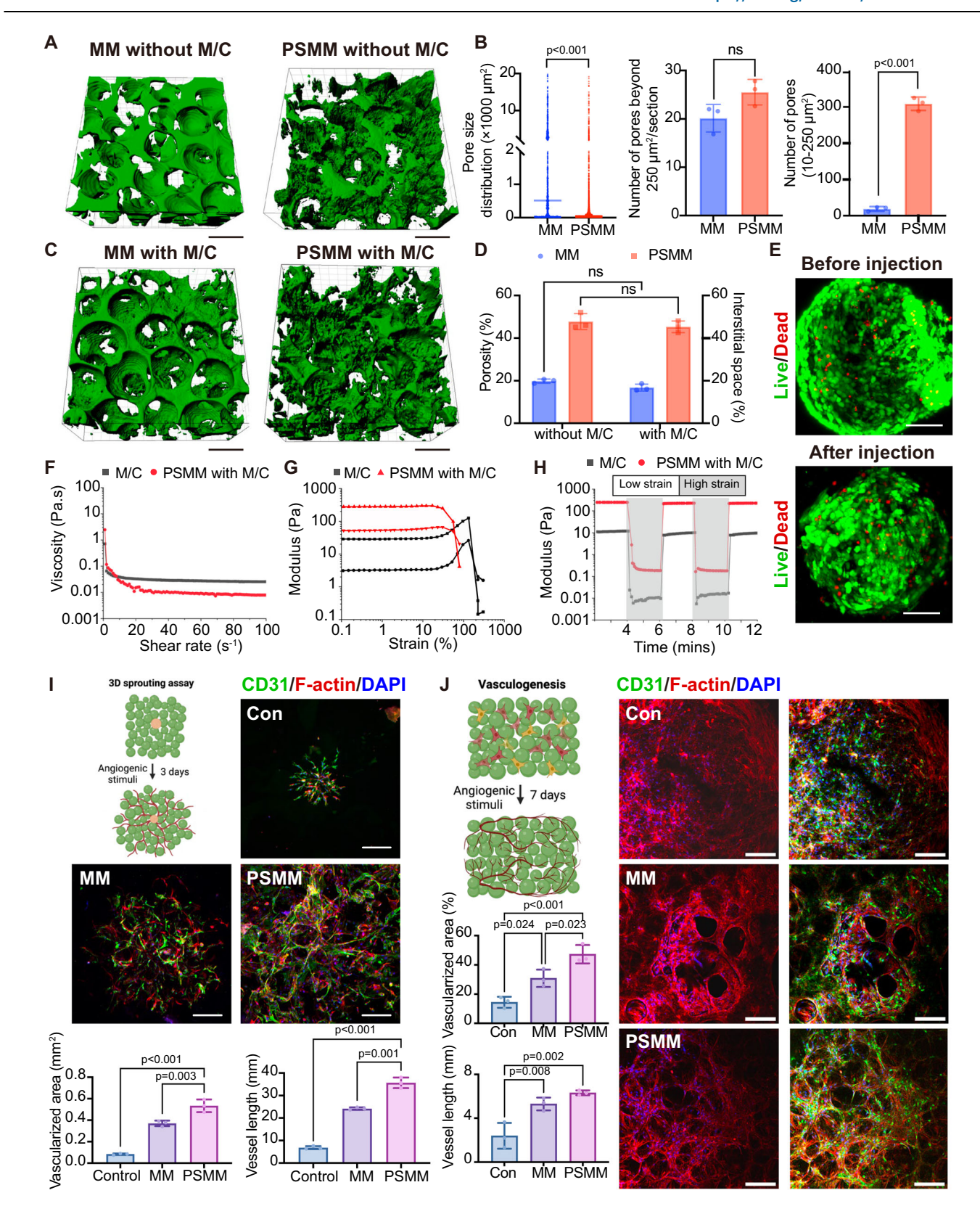
Microgel-matrix composite promotes EC vascularization

A critical step in angiogenesis involves the emergence of a specialized subset of ECs known as tip cells at the leading edge of vascular sprouts. These cells exhibit high migratory capacity, minimal proliferation, and numerous filopodia that sense microenvironmental cues³⁴. Endothelial sprouting from spheroids is a well-established indicator of tip cell activation and angiogenic initiation³⁰. In this study, we employed coculture spheroids of ECs and mesenchymal stromal cells (MSCs), a more physiologically relevant model than EC monocultures, as MSCs contribute to angiogenesis by stabilizing nascent vessels and remodeling the extracellular matrix, including collagen IV deposition^{35,36}. Based on this rationale, we embedded EC/MSC spheroids within PSMM scaffolds, MM scaffolds, and M/C mixtures (bulk hydrogel control) to assess EC sprouting (Fig. 31). Throughout the experimental period, the EC sprouting from spheroids increased in size and complexity (Supplementary Fig. 11). Confocal imaging of EC-specific marker CD31 was utilized to visualize EC sprouting within the scaffolds after 3 days of culture. Vascularized area and vessel length were enhanced in both microgel scaffolds, where the highest length presented in the PSMM scaffold as 1.48-fold longer than that in the MM group, demonstrating its superior pro-angiogenic capacity (Fig. 3I).

Furthermore, to investigate the vasculogenesis potential of microgel-matrix composites, the suspensions of ECs and human embryonic fibroblasts (HEFs) were mixed with the matrix prior to crosslinking (Fig. 3J). The vascularized area was notably increased in both microgel groups, with the PSMM scaffold exhibiting more extensive neovascularization, likely due to its interstitial space facilitating neovascular plexus formation. Considering the in vitro observation of vessel formation within the PSMM scaffold, we aimed to assess its angiogenic capacity in vivo and to determine if varying microgel sizes affected blood vessel formation. The first demonstration from animal studies exhibited promoted cell infiltration in both 200-μm and 400-μm in diameter of PSMM scaffolds (Supplementary Fig. 12). Examination of the EC marker CD31 indicated that PSMM scaffolds with 200-µm diameter presented a significantly higher number of CD31-expressing cells 14 days post-injection (Supplementary Fig. 13), likely due to optimized interstitial space facilitating greater cell migration into the scaffold.

Survival and differentiation of NPCs transplanted with PSMM scaffold are enhanced in stroke rats

The stroke cavity is a region that offers substantial plasticity and recovery following stroke, serving as an ideal transplant site to accept a large volume injection. To further assess the influence of scaffolds composition on NPC fate in vivo, green fluorescent protein-expressed NPCs (GFP-NPCs) were transplanted into the stroke cavity of rats



(coordinates of 0.3 mm posterior to the bregma, 3.5 mm lateral to the midline, and 1.8 mm below the skull surface) 7 days after distal middle cerebral artery occlusion (dMCAO, Fig. 4A and Supplementary Fig. 14). After 1 day of transplantation, only a few GFP-NPCs were observed when cells were directly injected with phosphate-buffered saline (PBS, Fig. 4B, C), whereas the M/C matrix modestly improved initial cell retention. However, both groups failed to maintain NPCs survival after

7 days of transplantation. In contrast, microgel-based delivery significantly enhanced cell retention, with the PSMM scaffold group exhibiting the highest number of surviving GFP-NPCs (3.44-fold and 1.63-fold greater than the PBS and MM groups, respectively). Notably, while NPC numbers in the MM group declined over time, the PSMM group maintained a cell density of 908.68 ± 65.45 cells mm⁻² at Day 28 (Fig. 4C).

Fig. 3 | **Interstitial space and injectability of microgel scaffolds, and promoted EC vascularization in vitro. A** 3D-rendered confocal images of MM and PSMM microgels. **B** Quantitative porosity comparisons between MM and PSMM microgels. **C** 3D-rendered confocal images of MM and PSMM microgels-M/C matrix composites. **D** Quantitative porosity or interstitial space of MM and PSMM microgels or MM and PSMM microgels-M/C matrix composites. **E** Live/dead (green/red) staining micrographs of NPCs cultured in PSMM with M/C matrix before and after injection. **F**-**H** Rheological properties of M/C and PSMM with M/C, including viscosities as a function of shear rate from 0 to 100 s⁻¹ (**F**), amplitude sweeps showing shear storage (triangle) and loss (inverted triangle) moduli as a function of shear stress at 37 °C (**G**), and continuous step strain sweeps from 1% to 500% at

 $37\,^{\circ}\text{C}$ (H). I 3D sprouting assay of ECs/MSCs embedded in microgels. Representative florescence micrographs displaying CD31 (green) and F-actin (red) of embedded cells on Day 3. And the corresponding quantitative results of vascularized area and vessel length. J Vasculogenesis experiment of ECs and HEFs cultured in microgels. Representative florescence micrographs showing CD31 (green) and F-actin (red) of ECs on Day 7, with quantitative results for vascularized area and vessel length. Scale bars, **A**, **C**, I and J, 200 µm; **E**, 50 µm. Data are mean values \pm SDs. **B**, n=3 technically independent samples, unpaired t test; **D**, n=3 technically independent samples, one-way ANOVA; J, n=3 technically independent samples, one-way ANOVA. ns no significant difference. Source data are provided as a Source Data file.

Cell distribution of transplanted NPCs also differed markedly across conditions. Cells delivered in PBS and M/C appeared compact and densely packed, whereas those in microgel conditions were more broadly dispersed throughout the transplantation area (Fig. 4B). The reduced cell numbers in the PBS, M/C, and MM groups might be attributed to cellular apoptosis caused by an unfavorable microenvironment and insufficient voids for cell survival and proliferation. To assess the cellular apoptosis, terminal deoxynucleotidyl transferase dUTP nick end labeling (TUNEL) method was conducted. As shown in quantification of TUNEL+/GFP+ cells (Fig. 4D and Supplementary Fig. 15), on Day 1 post-transplantation, a large proportion of GFP⁺ cells were labeled with TUNEL in the PBS, M/C, and MM groups. TUNEL+/ GFP+ cells were rarely observed within injected area 7 days posttransplantation. These findings suggest that the PSMM microgel scaffolds provide a supportive physical environment conducive to longterm NPC survival post-transplantation.

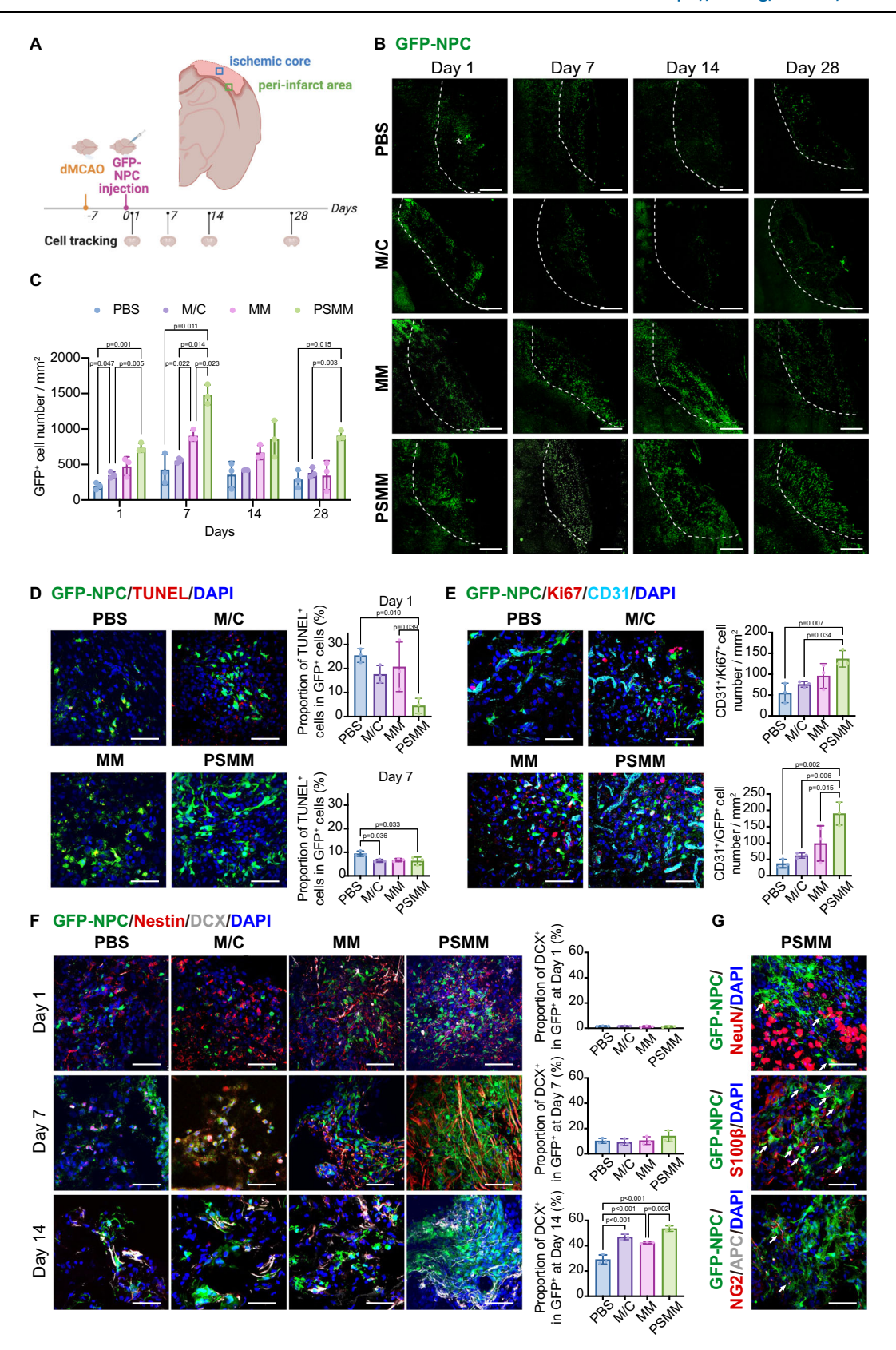
To study the influence of microgel scaffolds on NPC proliferation in vivo, brain sections were stained for the Ki67 at 7-, 14-, and 28-days post-transplantation. As compared with all other conditions, PSMM scaffolds exhibited significantly higher proliferation after 7 days (Fig. 4E). Interestingly, immunostaining results for Ki67⁺/CD31⁺ cells indicated enhanced EC proliferation within the stroke cavity when NPCs were delivered using the PSMM scaffold. Among these Ki67⁺/CD31⁺ cells, the co-localization with GFP-NPCs was observed in the PSMM group, suggesting that NPC proliferation could potentially associate with concurrent EC proliferation and infiltration.

Our objective for damaged tissue repair is to support the differentiation of NPCs into neurons while also sustaining the viability of transplanted cells. Thus, differentiation of transplanted GFP-NPC was further evaluated by co-staining cells with Nestin, doublecortin (DCX), and NeuN, which are markers for NPCs, immature neural precursors, and mature neurons, respectively. Over the 28-day period following NPC transplantation, the proportion of Nestin⁺ cells in GFP-NPCs decreased, and the DCX+ immature neural precursors were increased (Fig. 4F and Supplementary Figs. 16-19), suggesting that the transplanted NPCs were differentiating toward a neuronal lineage. In the ischemic core area, the highest proportion of DCX+ cells in GFP-NPCs $(53.54 \pm 2.15\%)$ was observed in PSMM group at 14 days post-injection. Meanwhile, migrated GFP+ cells were observed over a broader periinfarct area outside the injection site at 14 days post-transplantation (Supplementary Figs. 16 and 17), displaying differentiated morphology (DCX⁺), indicating their potential integration into the host tissue. We further stained for NeuN, a neuron-specific marker, to determine whether the increased NPC population was differentiating into neurons. As shown in Fig. 4G and Supplementary Fig. 20, NeuN⁺/GFP⁺ cells were observed within the ischemic core of both microgel groups at 28 days post-transplantation. However, the PSMM group presented a significantly higher proportion of NeuN⁺ cells compared to the MM group, with $19.12 \pm 3.19\%$ in ischemic core and $33.54 \pm 5.41\%$ in periinfarct area. This observation suggests that encapsulating NPC in PSMM scaffolds enhances their differentiation beyond the progenitor state more effectively than previously described approaches³⁷. Considering the multilineage differentiation capacity of NPCs, the other cell types were also evaluated at 28 days post-transplantation. Besides neurons, another major cell type of $S100\beta^+/GFP^+$ astrocyte was differentiated, and only a small proportion of $NG2^+/GFP^+$ oligodendrocyte precursor cells and few of APC+/GFP+ oligodendrocytes were observed (Fig. 4G and Supplementary Fig. 21).

Transplantation of NPCs with microgel-matrix composites increases vascularization and reduces glial scar formation, facilitating neurological functional recovery in ischemic stroke rats

Microgel-matrix composites provide pathways for cell migration, prompting us to investigate whether various endogenous cell types could infiltrate the stroke core through these interstitial spaces. We observed vessel infiltration into the stroke cavity, with a statistically significant difference between the microgel-treated brains and the PBS and M/C-treated groups at 7 days post-transplantation (Fig. 5A). These infiltrating vessels may have contributed to the enhanced survival and proliferation of NPCs during the long-term recovery period. In the PSMM group, CD31⁺ area and vessel junction numbers were markedly increased (Supplementary Fig. 22), indicating a denser and more branched vascular network, likely due to enhanced angiogenic remodeling³⁸⁻⁴⁰. During the remodeling phase, angiogenesis leads to the formation of capillaries with greater branching complexity, ultimately restoring microcirculatory function^{39,40}. The vascular features observed in the PSMM group are consistent with this remodeling phase, suggesting that the PSMM scaffold may facilitate a more mature and functional vascular network. To determine whether astrocytes also infiltrate through the interstitial spaces, we assessed glial responses at Day 28 post-transplantation. Both glial scar thickness and the integrated optical density (IOD) of GFAP+ astrocytes surrounding the stroke core were significantly reduced in the PSMM group (Fig. 5B and Supplementary Fig. 23), indicating an attenuated astrocytic response and suggesting a more permissive environment for neural tissue integration.

Furthermore, by applying the rotarod test, modified neurological severity score (mNSS), and elevated body swing test (EBST), we examined neurological behaviors to determine whether NPC transplantation with PSMM scaffold promotes more effective functional recovery than NPC transplantation with MM group. The rotarod test measures motor coordination and balance. After stroke, rats exhibited a dramatically shorter time on the rotarod compared to shamoperated animals (Fig. 5C). On Day 14 post-transplantation, only rats receiving NPCs in PSMM scaffold showed a prolonged duration on the rotarod compared to their pre-transplantation performance, with this improvement persisting through Days 14 to 28. The EBST was also employed to assess asymmetrical motor behavior. The stroke-induced rats initially showed a 100% tendency to turn towards the right (Fig. 5D). On Days 21 and 28, the PSMM scaffold group demonstrated a significantly reduced percentage of right-biased swings, while no significant changes were observed in other groups over the 28-day period. Finally, the mNSS test was applied to assess the rat motor abilities, reflexes, and balance. On Day 28 post-transplantation, rats received PSMM scaffold exhibited lower mNSS scores compared to the PBS and



bulk hydrogel groups (Fig. 5E), with a decreasing trend also observed compared to the MM group. To further verify the consequence of hydrogel transplantation on stroke-induced brain atrophy, we assessed the atrophy volume on Day 28 utilizing cresyl violet staining. The brain atrophy volume in the PSMM group was considerably smaller than that in the PBS group by 40.93% (Fig. 5F).

Collectively, these data demonstrate that the microporous structure of the microgel is critical for transplanted NPC residency, vessel and astrocyte infiltration, as well as for reducing scar thickness in the infarct core. Enhanced neurogenesis and vasculature were not confined to the infarct boundary but extended throughout the infarct core. Additionally, NPCs exhibited significantly greater colocalization

Fig. 4 | **PSMM** scaffolds enhance the survival and differentiation of transplanted NPCs in stroke rats. A Schematic of experimental timeline and brain region selection for analyses after ischemic stroke. **B** Overview of a brain section showing the ipsilateral region of dMCAO and transplanted GFP-NPCs (green). The dish line marks the boundary of the stroke cavity, and the asterisk indicates the stroke cavity. Experiment was independently repeated three times with similar results. **C** Quantitative results of GFP+ cell numbers on Days 1, 7, 14, and 28 post-transplantations. **D** Representative florescence micrographs presenting GFP-NPC (green) and TUNEL (red) in ischemic cores on Day 1 after transplantation. And the corresponding quantitative results of TUNEL+ cell percentages. **E** Representative florescence micrographs showing GFP-NPC (green), Ki67 (red), and CD31 (light blue) in ischemic cores on Day 14 after transplantation, with corresponding

quantitative results of CD31*/Ki67* cell numbers and CD31*/Ki67* co-localization. **F** Representative florescence micrographs presenting GFP-NPC (green), Nestin (red), and DCX (gray) in ischemic cores on Days 1, 7, and 14 after transplantation. And the corresponding quantitative results of DCX* percentages on Days 1, 7, and 14 after transplantation. **G** Representative florescence micrographs of GFP-NPC (green) and NeuN (red), S100 β (red), or NG2 (red) and APC (gray) in ischemic cores on Day 28 after transplantation of PSMM group. Arrows indicating NeuN*, S100 β *, or NG2* and GFP* cells. Experiment was independently repeated three times with similar results. Scale bars, **B**, 500 μ m; **D**–**G**, 100 μ m. Data are mean values \pm SDs. **C**, n=3 mice; two-way ANOVA; **D**, n=3 mice, one-way ANOVA; **E**, n=3 mice, one-way ANOVA; **E**, n=3 mice, one-way ANOVA. Source data are provided as a Source Data file.

with vasculature in the PSMM group compared to the MM group. These processes, encompassing neurogenesis and angiogenesis, are critical for promoting revascularization and providing neuroprotective effects after ischemic stroke.

Discussion

Hydrogel scaffolds are extensively used for stem cell delivery in treating various diseases. However, the impact of voids within hydrogels on stem cell viability and function remains unclear. Transplanting hydrogels with NPCs for brain repair is particularly challenging, as NPCs are susceptible to the adverse conditions of the injured microenvironment. Our findings highlight the critical role of the microstructure induced by phase-separation of microgel sustaining NPC viability and function in such contexts. In this study, the PSMM scaffold, formed using ATPS hydrogel, exhibited superior cell-loading capability, significantly enhancing NPC viability. Unlike traditional microgels, which typically restrict cells to their surfaces (as reported in previous studies^{18,41}), our pore-forming microgel allowed NPCs to infiltrate and fill the entire microgel volume after 7 days of culture (Fig. 2], K and Supplementary Fig. 8). This difference is attributed to the interconnected microporous structure of the PSMM microgel, providing adequate space for cell proliferation and migration. Exemplary emulsion hydrogel showed in this study is alginate and PVA, yet broad combinations based on various applications can be designed according to different requirements.

The survival, proliferation, and differentiation of NPCs were also confirmed through transplantation experiments conducted on ischemic rats. The enhanced survival of exogenous NPCs was observed up to 28 days after transplantation in Fig. 4B. Notably, this long-term survival of transplanted NPCs in the stroke cavity with equal distribution is unprecedented. Neuronal differentiation (Fig. 4G and Supplementary Figs. 16–20) and long-term neurological recovery (Fig. 5C–E) were also evident. While most previous studies have focused on engineering hydrogels with peptide motifs or growth factors to recruit endogenous stem cells⁴², the PSMM scaffold's porosity provides a supportive microenvironment that directly enhances exogenous cell proliferation. Its unique porous structure increases the surface area-tovolume ratio, allowing for more efficient diffusion and better cell integration compared to bulk hydrogels. Although neuronal differentiation is notably improved in the PSMM group, astrocytic fate remains the dominant lineage outcome. Further investigation is needed to develop strategies, such as transcription factor-mediated programming to promote more efficient neuronal differentiation of transplanted NPCs in vivo.

Effective brain repair following ischemic stroke requires not only neuronal replacement but also coordinated angiogenesis and vascular remodeling to restore oxygen and nutrient supply^{43,44}. To meet this challenge, we designed a PSMM microgel-matrix composite that integrates two critical functions: a microporous microgel interior that supports stem cell proliferation, and an interstitial matrix that facilitates EC migration and vascular growth. Although our microgel-matrix composite design sacrifices some inter-microgel porosity, it

achieves enhanced functional integration by combining a proliferation-permissive microgel interior with an angiogenesissupportive interstitial matrix. As illustrated in Fig. 3I, J, the interstitial space of PSMM scaffolds effectively guided vascular network patterning and regulation in vitro, which is aligned with previous studies^{19,45,46}. In the absence of matrix, PSMM exhibited significantly higher porosity than MM scaffolds, particularly in the small-pore range. Upon incorporation of the M/C matrix, these small voids were occupied by M/C matrix as interstitial spaces that supported vessel infiltration and remodeling, thereby enhancing the biological activity essential for tissue regeneration. In vivo experiments also confirmed these findings, as CD31 staining demonstrated EC infiltration into the scaffolds. The ECs and transplanted NPCs grew concomitantly during regeneration process (Fig. 4E), highlighting the close interaction between these two cell types. Migrating ECs paved the way for transplanted NPCs to infiltrate the peri-infarct region while forming functional vasculature to nourish the transplanted cells. Simultaneously, NPCs within the stroke cavity likely secreted trophic factors to guide EC migration, further supporting vascular remodeling and tissue repair.

Of note, glial scar, a barrier formed by astrocytes to prevent further damage but which obstructs regeneration, was significantly reduced in PSMM group (Fig. 5B and Supplementary Fig. 23). Enhancing the infiltration of pro-regenerative astrocytes into the infarct area could therefore promote recovery after ischemic stroke^{47,48}. Following stroke, reactive astrocytes form a glial scar that hinders neurite regeneration and functional recovery through a physical and chemical barrier. As expected, PBS-treated animals exhibited a pronounced glial scar thickness, whereas injection of the microgels into the stroke cavity significantly reduced the scar thickness. This result aligns with findings from a previous study, where a hyaluronic acid-based microporous annealed particle hydrogel similarly reduced glial scarring when injected into the stroke cavity²¹. The augmented infiltration of reparative astrocytes into the hydrogel scaffold likely contributed to the reduced astrocyte accumulation in the surrounding area. Similarly, the reduction of this barrier promoted EC infiltration into the scaffold (Fig. 5A). However, further studies are required to determine whether the infiltration of ECs and astrocytes occurs simultaneously or sequentially.

Although identifying microgels with a pore-forming structure is a critical first step in advancing stem cell therapy, particularly in demonstrating their ability to promote stem cell survival and regulate differentiation, there are three major limitations to this study. First, careful consideration must be given to microgel degradation, as the degradation timeline may hinder further cell infiltration into the stroke area. It has been suggested that the degradation of alginate-based microparticles occurs slowly, providing long-term support for cells^{49,50}. Future investigations should focus on determining whether the degradation of microgel is influenced by the size of the pores or by the encapsulated cells. Furthermore, Matrigel has been extensively utilized in diverse cell culture applications, due to its ease to use, availability, and versatility in supporting the growth of various cell

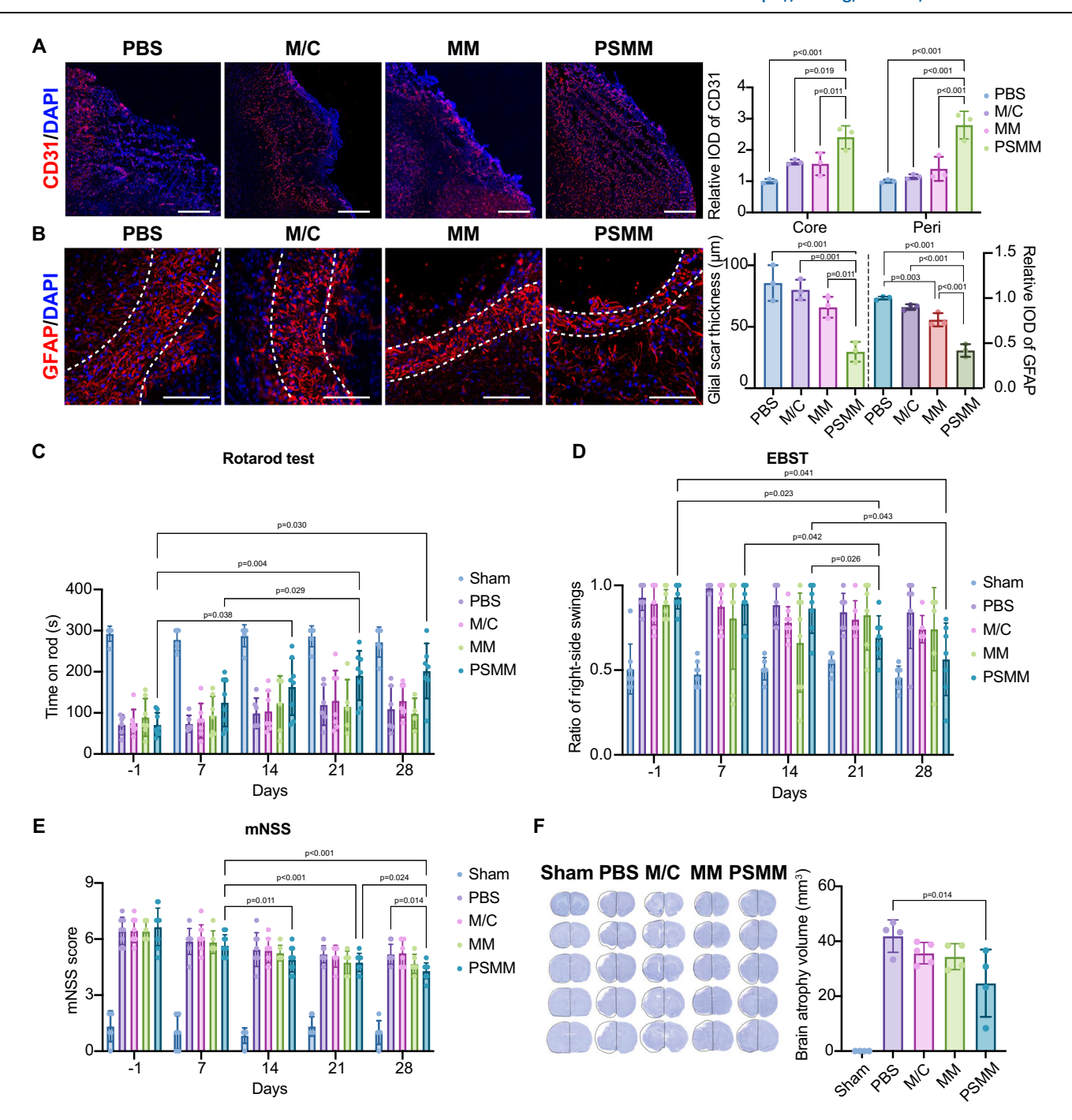


Fig. 5 | **Transplantation of NPCs with PSMM scaffolds promotes neurological functional recovery of ischemic stroke rats. A** Representative florescence micrographs of CD31 (red) in brain sections on Day 28 after transplantation. And the corresponding quantitative results of CD31 integrated optical density (IOD) in the ischemic core and peri-infarct regions. **B** Representative florescence micrographs representing GFAP (red) in brain sections on Day 28 after transplantation, with corresponding quantitative analysis of glial scar thickness and GFAP IOD. The dashed line represents the boundary of the glial scar. C–E Neurological behavior assessments of dMCAO rats following microgel injection, including the EBST (**C**), rotarod test (**D**), and mNSS (**E**) conducted on Days 1, 7, 14, and 28 post-transplantation. In the EBST, normal rats typically exhibit a right-side swing ratio of approximately 0.5, whereas stroke rats, due to left-sided brain injury, display a

rightward bias. In the rotarod test, the maximum duration is 300 s, with longer times indicating superior motor function. The mNSS ranges from 0 to 12, with higher scores denoting greater neurological impairment. **F** Images of rat brains and cresyl violet-stained brain sections on Day 28 post-transplantation, and quantitative results of brain atrophy volume. Dashed lines indicate brain atrophy. Scale bars, **A**, 500 μ m; **B**, 100 μ m. Data are mean values \pm SDs. **A**, n = 3 mice, two-way ANOVA; **B**, n = 3 mice, two-way ANOVA; **C**, n = 6, 6, 7, 7, and 8 mice for Sham, PBS, M/C, MM, and PSMM group respectively, two-way ANOVA; **D**, n = 8, 7, 8, 8, and 8 mice respectively, two-way ANOVA; **F**, n = 4, 4, 5, 4, and 4 mice respectively, one-way ANOVA. Source data are provided as a Source Data file.

types. However, the poorly understood composition and variations of Matrigel have led to uncertainty in cell culture, as well as the following regenerative applications. Recent progress of synthetic materials development provides alternatives that are well-defined and

reproducible⁵¹. Additionally, it is important to mention that the in vivo studies conducted as part of this work are restricted due to the use of small animal models. While the advantages of the current rat model include rapid feedback from experiments and ease of manipulation,

we acknowledge that the current protocol oversimplifies the surgical procedure. Moving forward, the conclusion will have to be based on additional evidence gathered from preclinical studies using larger animal models in the future.

Overall, the PSMM scaffold emerges as a highly promising platform for stem cell encapsulation, offering an integration of a high-throughput air-microfluidic fabrication process and in vivo inject-ability. This pore-forming microgel scaffold, featuring both internal microporosity and interstitial matrix, addresses stem cell delivery challenges in stroke therapeutic methods by significantly enhancing NPC survival and neuronal differentiation in vivo. Beyond neural repair, the interstitial matrix also promotes vascular regeneration. These insights into NPC behavior post-transplantation provide a strong foundation for developing innovative therapies targeting neurodegenerative diseases, where targeted neuronal replacement and neurovascular support are therapeutic priorities. By bridging the gap between scientific innovation and clinical translation, this platform represents a significant step forward in the field of tissue engineering and regenerative therapy.

Methods

Preparation of aqueous two-phase emulsion (ATPM) hydrogel

The formation of ATPM hydrogel was prepared following the modified methods as we previously reported $^{25\text{-}27}$. Briefly, 2 wt.% sodium alginate (Sigma-Aldrich, USA) was mixed with 10 wt.% Poly (vinyl alcohol) (PVA, M_w = 89–98 kDa, Sigma-Aldrich) to achieve final concentration of 3, 4, or 5 wt.% PVA and 0.75 wt.% sodium alginate. The micropore-forming hydrogel was prepared through vigorous vortexing. The size distribution of PVA droplets in the sodium alginate solution was measured right after the emulsion was formed, using Measure Tool in ImageJ software (National Institutes of Health, USA).

Fabrication of microporous microgel (MM) and phase-separated microporous microgel (PSMM) with different sizes

The gas-shearing microfluidic device was set up based on the previously studies⁵²⁻⁵⁴, and illustrated in Fig. 2B and Supplementary Fig. 3A. To prepare the hydrogel precursor solutions, 2 wt.% sodium alginate was dissolved in PBS, while PVA was separately dissolved in PBS with heating and stirring. The final pore-forming formulation consisted of 0.75 wt.% sodium alginate and 5 wt.% PVA. Before adding into the fabrication device, the mixed solution was vortex for 8 s to ensure uniform emulsification. During fabrication, hydrogel solution was injected into the air microfluidic device at a flow rate of 18 mL h⁻¹. Microgel droplets were generated by gas-shearing once the applied gas pressure overcame the surface tension of the aqueous phase. Upon contact with the calcium ion-containing collection bath, alginate crosslinked rapidly while PVA remained in liquid form. As PVA diffused out of the gel matrix over time, it left behind interconnected pores in the regions it previously occupied. To generate microgels with varying diameters, the nitrogen gas flow rate was adjusted to 0.6, 0.8, or 1.2 L min⁻¹ to produce large, medium, and small microgels, respectively. Meanwhile, we used 0.75 wt.% sodium alginate as a MM formulation and the other parameters are consistent with those of PSMM. The size distribution of microgels was analyzed by the Measure Tool in the ImageJ software.

Packing of microgels into injectable scaffolds

To pack microgels into the injectable scaffold, microgels were first centrifuged to remove excess supernatant. An equal volume of M/C mixture was then added and gently mixed to ensure uniform distribution. The resulting mixture was incubated at 37 °C for 30 min to achieve thermal crosslinking and scaffold stabilization. For comparative studies evaluating scaffold porosity in the absence of M/C, microgels were directly transferred into molds after centrifugation, without the addition of any matrix. For in vivo applications, the

microgels mixed with M/C solution were maintained on ice prior to injection to preserve the pre-gel state.

Fabrication of microgel with traditional microfluidic method

To compare efficiency of traditional microfluidic method with gasshearing method, we utilized the same gas-shearing fabrication condition with the one of 0.75 wt.% sodium alginate to obtain MM. The 0.75 wt.% sodium alginate solution as the exemplary was injected under the flow rate of 18 mL h⁻¹, and the flow rate of nitrogen was 1.2 L min⁻¹. For the fabrication procedure of traditional microfluidic method, a microfluidic device was developed based on the previous study (Supplementary Fig. 3B)55. Briefly, the microfluidic chip was composed of two 200-µm microchannels, which form a 90° T-junction. As the dispersed phase in vertical channel flows through this T-junction, the droplets were generated with the shear force of continuous flow in horizontal channel. The 10 wt.% GelMA solution was used as dispersed phase and injected with 100 µL min⁻¹ of flow rate, and paraffin liquid with 8 wt.% mineral oil was applied as continuous phase and injected with 2.5 µL min⁻¹ of flow rate. The microgels were fabricated by these two methods and collected for 10 min.

Characterization of microgel scaffolds

Porosity characterization: The microgels were collected into an Eppendorf tube, centrifuged at $315 \times g$ for 3 min, and removed the supernatant. Next, the microgels suspended in collagen I (2 mg mL⁻¹, pH = 7, Gibco, USA) and Matrigel (Corning, USA) solution (at a volume ratio of 3:1) containing 5 mg mL⁻¹ FITC-dextran (M_w = 2000 kDa, Sigma-Aldrich) was used to characterize the porosity. The hydrogel was fully mixed and transferred to the polydimethylsiloxane (PDMS, 10:1, Sylgard 184, Dow Corning, USA) mold, incubated at 37 °C for 30 min to achieve scaffold stabilization. The sample was then covered with a glass coverslip, and imaging was performed using a laser scanning confocal microscope (Carl Zeiss, LSM880, Germany) to visualize the FITC-dextran within the interstitial pores and microgels. Microscopy files were further analyzed in Imagel software. Fluorescent signals in each slice were first smoothed to reduce noise and then thresholded for further analysis. The area fraction of the fluorescent signal, total number and cross-sectional area of pores was obtained using the Analyze Particles function. 3D porosity within granular hydrogels was visualized by IMARIS software. The surfaces feature was used with surface grain size of 2.5 µm and diameter of largest sphere of 30 µm to recreate volumetric pores.

Rheological evaluation: An oscillatory shear rheometer (MARS 40, ThermoFisher, USA) was used to evaluate the rheological properties of granular hydrogels with a 20 mm parallel steel plate geometry and a 1 mm gap. Viscosity was assessed by applying a continuously ramped shear rate ranging from 0 to $100\,\mathrm{s^{-1}}$ to characterize flow behavior. Strain sweeps (1–1000% strain, 1 Hz) were conducted to evaluate shear-yielding properties. Additionally, shear recovery was assessed by alternately applying low (1%) and high (500%) strains every 2 min at 1 Hz.

Evaluation of PVA removal from microgels

For assessing PVA removal from microgels, we utilized rhodamine B-labeled PVA (QIYUE Biology, China), which served as both a fluorescent marker for visualization and a quantitative probe by measuring its release into solution^{29,56}. A pore-forming hydrogel was prepared with a final composition of 0.75 wt.% GFP-sodium alginate and 5 wt.% rhodamine B-labeled PVA. For the preparation of PSMM microgels, the nitrogen flow rate was set at 1.2 L min⁻¹, and a 0.5 wt.% calcium chloride solution was used as the crosslinking bath, positioned 10 cm below the nozzle to collect printed microgels. Immediately after printing, the calcium chloride solution containing the microgels was collected. At designated time points (0 min, 30 min, 1 h, 4 h, and 24 h post-fabrication), aliquots of the supernatant were aspirated and analyzed at

562 nm using a microplate reader (Tecan, Switzerland) to quantify the released rhodamine B-labeled PVA. Simultaneously, microgels were harvested at the same time points and imaged using a confocal laser scanning microscope (FV3000, Olympus, Japan) to qualitatively assess the fluorescence intensity of retained rhodamine B-labeled PVA within the microgel-matrix.

Fabrication of neural progenitor cell (NPC)-loaded MM and PSMM by gas-shearing

After attained confluence, NPCs were centrifuged and resuspended with alginate or alginate/PVA mixed solution at a density of $1\times 10^7~{\rm mL^{-1}}$. Experimental parameters as follows: Flow rate of the mixed solution was $18~{\rm mL~h^{-1}}$, and the flow rate of nitrogen was $1.2~{\rm L~min^{-1}}$. Hereafter, the microgels were washed with NPC medium for several times, and then kept in culture at $37~{\rm ^{\circ}C}$ with a $5\%~{\rm CO_2}$ humidified atmosphere incubation.

Scanning electron microscopy (SEM) of microgels

Microgels were fixed using glutaraldehyde and prepared for SEM following a standard dehydration and drying protocol⁵⁷. Briefly, samples were fixed in 2.5 wt.% glutaraldehyde for 1 h at room temperature, following the washing with calcium-containing PBS buffer (pH = 7.2) for 1 h for 3 times. Then, gradual dehydration was performed using a graded ethanol series (30, 50, 70, 80, 90, and 100 wt.%). Sample were immersed in each ethanol concentration for 15 min. After dehydration, samples were dried for 1 h using a critical point dryer to avoid surface tension-induced deformation. After drying, samples were sputtercoated with a thin layer of gold (10 nm) and imaged using a scanning electron microscope.

The injectability evaluation of microgel scaffolds

Following established methodology, we adopted injecting length through a nozzle as a reliable measure of microgel injectability 58 . Microgels were centrifuged at $315\times g$ for 3 min, and the supernatant was completely removed. An equal volume of M/C solution was then added to the microgels and mixed thoroughly. The mixture was kept on ice prior to injection. For the group without M/C, microgels were directly transferred to a syringe after centrifugation and supernatant removal. A syringe equipped with a needle of 500 μ m inner diameter was used to extrude the microgel scaffolds at a constant rate of 5 μ L min $^{-1}$, which is consistent with animal experiments. The extrusion process was recorded, and the filament lengths extruded within 50 s were quantified.

Evaluation of cell distribution within microgels

To assess the uniformity of cell distribution, microgels cultured for 7 days were fixed in 4 wt.% paraformaldehyde (PFA) for 15 min and washed three times with calcium-containing PBS. The samples were stained with 4′,6-diamidino-2-phenylindole (DAPI, $1\,\mu g\,mL^{-1}$, YEASEN, China) in calcium-containing PBS for 10 min. Z-stack images were acquired using an FV3000 confocal microscope, capturing 20 slices with a z-interval of 10 μm . For quantitative analysis, four interslice planes with 40 μm spacing were selected from each group (MM: Z = 4.33, 4.37, 4.41, 4.45 mm; PSMM: Z = 4.27, 4.31, 4.35, 4.39 mm). Each selected slice was divided into four quadrants, and the number of cells per quadrant was counted using ImageJ.

Investigation NPC survival and proliferation in vitro

The NPC viability loaded in microgel was measured with a Calcein-AM/PI Double Staining kit (ThermoFisher). At designed time point, the microgels were collected and centrifuged to remove the supernatant. The working solution (2- μ M Calcein AM and 8- μ M PI) was added, followed by the incubation at 37 °C away from light for 15 min. Images were captured with confocal microscope (FV3000) immediately after staining. Image processing and analysis were conducted in Imagel software.

Cell proliferation was assessed after cultured for 1, 3, 5, and 7 days, followed by evaluation of MTS Cell Proliferation Assay Kit (YEASEN, China). 200- μ L microgel suspension was mixed with 20- μ L MTS working solution (5 mg mL⁻¹), and incubated for 4 h. After centrifuging at 315 × g for 3 min, 100- μ L formazan solution was added to each well and incubate for extra 4 h. Following that, the optical density was measured at 570 nm utilizing a microplate reader (Tecan, Switzerland).

Immunofluorescence staining was performed to evaluate the expression of key markers for NPCs and differentiated cells. First, the microgels loaded with cells were fixed using 4 wt.% PFA and then permeabilized with a 0.3 wt.% Triton ×-100 solution. After blocking with 1 wt.% BSA, the microgels were incubated overnight at 4 °C with primary antibodies: mouse anti-Nestin (1:400, Millipore) and rabbit anti-Ki67 (1:400, Abcam). The microgels were subsequently washed three times with calcium-containing PBS and incubated with the appropriate secondary antibodies for 2 h at room temperature. Nuclei were stained with DAPI in calcium-containing PBS at room temperature. Fluorescence images were captured using a fluorescence microscope, and the quantification was carried out using Measure Tool in ImageJ software.

Evaluating angiogenesis and vascularization of endothelial cells (ECs) in vitro

Human MSCs (ZOXZBio, China) and human umbilical vein endothelial cells (HUVECs, ZQXZBio, China) were dissociated into single-cell suspensions by incubation with 0.05% Trypsin-EDTA (Gibco) at 37 °C. Cells were mixed in a HUVEC: MSC = 2:1 ratio, and cell suspensions containing both types of cells were added to Aggrewell-400 (Stemcell, USA) for overnight culture. Preparation of a matrix for vascularization by mixing collagen I (2 mg mL⁻¹, pH = 7) and Matrigel at a volume ratio of 3:1 on ice. The prepared microgel was gently centrifuged and remove the supernatant. The microgel and matrix were mixed at a volume ratio of 1:1 and immediately transferred to the PDMS mold for gelation at 37 °C. The cell spheroids generated by Aggrewell were transferred into this M/C mixture, and were further cultured in EC culture medium (Lonza, Swiss) supplemented with 100-ng mL⁻¹ vascular endothelial growth factor (VEGF), 500-nM S1P, and 600-ng mL⁻¹ phorbol myristate acetate (PMA) for 3 days, as previously reported³⁶. These samples were fixed and stained with CD31 (Abcam), PhalloidiniFluor 555 (Abcam), and DAPI. The stained images were captured by fluorescence microscope and the quantification of total vessel length and vascularized area was conducted by the Manual Tracking Tool of Imagel software.

In vitro vascularization was evaluated by ECs and HEF cells based on the principle of vasculogenic self-assembly. The microgel-matrix was prepared same as last step, and two cells with different concentrations (HUVEC = $3 \times 10^6\, \text{mL}^{-1}$, HEF = $6 \times 10^6\, \text{mL}^{-1}$) were introduced and fully mixed with microgel-matrix. After gelation in 37 °C, these samples were further cultured in EC culture medium supplemented with 100-ng mL⁻¹ VEGF, 500-nM S1P, and 600-ng mL⁻¹ PMA for 7 days ^{59,60}, changing medium every two days. These samples were fixed and stained with CD31, Phalloidin-iFluor 555, and DAPI. The stained images were captured by fluorescence microscope, and the quantification was conducted by ImageJ software. The area of the scaffolds was measured on Days 0, 1, 3, 5, and 7 using ImageJ software.

Assessment of cell viability after injection

We centrifuged the microgels at $315 \times g$ for 3 min, completely removed the supernatant, and then added an equal volume of M/C solution to the microgels volume. After thoroughly mixing, the mixture was placed on ice for later injection. For the group without M/C, after centrifugation and removal of the supernatant, the microgels were directly transferred to a syringe for injection. A syringe needle of $500 \, \mu m$ inner diameter was used to inject the scaffolds at a flow rate of $5 \, \mu L \, min^{-1}$. Following injection, microgels were collected and were measured with a Calcein-

AM/PI Double Staining kit (ThermoFisher). The working solution (2- μ M Calcein AM and 8- μ M PI) was added, followed by the incubation at 37 °C away from light for 15 min. Images were captured with confocal microscope (Olympus) immediately after staining. Image processing and analysis were conducted in ImageJ software.

Distal ischemic stroke model (dMCAO) induction

Adult Sprague-Dawley rats $(280-310 \times g, 7-8 \text{ weeks old, male, } n=31$ per group, 5 groups in total) were used, and were purchased from Charles River Laboratories (Shanghai, China). Animal anesthesia was induced and maintained with 2% isoflurane. Under a surgical microscope, a 2-cm vertical incision was made between the left orbit and ear. The temporalis muscle was bluntly dissected to expose the temporal bone, and the skull was thinned at the junction of the zygomatic arch and the squamosal bone using a cranial drill until translucent. The skull was carefully removed with curved forceps, and after excision of the dura mater, the middle cerebral artery (MCA) was exposed. MCA occlusion was performed through electrocoagulation, ensuring no damage to the surrounding brain tissue, and blood flow interruption was confirmed under a microscope. Subsequently, both common carotid arteries were ligated for 1 h to further reduce whole cerebral blood flow (CBF), after which circulation was restored by removing the ligatures. CBF was measured using a laser Doppler flowmeter (Moor Instruments, Devon, UK) to confirm the success of the model, with post-electrocoagulation blood flow reduced to 10% of baseline. In the sham-operated control group, all procedures were identical except for MCA occlusion.

Investigation NPC survival and proliferation in vivo

After surgery, the rats were randomly divided into four groups: NPC in PBS $(1 \times 10^6 \text{ cells in } 50 \,\mu\text{L PBS})$, NPC in M/C $(1 \times 10^6 \text{ cells in } 50 \,\mu\text{L})$ solution: Matrigel: collagen I=1:3), NPC in MM scaffold, and NPC in PSMM scaffold (microgels were distributed in equal volumes of M/C). Similarly, the rats were anesthetized with 2% isoflurane and secured in a stereotaxic injection apparatus (RWD, Shanghai, China). After disinfecting the head, the skin was incised to separate the periosteum and expose the skull. A small hole was drilled in the skull using a drill bit while irrigating with PBS to prevent overheating. A small hole was drilled in the skull using a drill bit while irrigating with PBS to prevent overheating. A syringe needle with inner diameter of 500 µm (Fuying, China) was employed to inject the therapeutic substance into the infarct cavity at the following coordinates: 0.3 mm posterior to the bregma, 3.5 mm lateral to the midline, and 1.8 mm below the skull surface, with an injection volume of 50 µL over 10 min. After 5-min pause, the needle was slowly withdrawn to prevent the injected substance from leaking out. After the injection, the skin was sutured, and the wound was disinfected to maintain sterility and promote healing. To prevent solidification and blockage of the needle, the microgels and solvents were maintained on ice during the surgery.

Neurological behavior evaluations

Behavioral tests were conducted from 1 day before injection to 28 days post-injection: mNSS, rotarod test, and EBST. Behavioral assessments were performed by a researcher blinded to the experimental design and group assignments. The mNSS was used to evaluate the overall motor and balance functions in rats, with scores ranging from 0 to 12, where a higher score indicates more severe motor function impairment. The Rotarod Test evaluates changes in motor coordination and balance. Prior to surgery, rats underwent continuous training for 3 days, with three sessions per day lasting 300 s each. The training speed gradually increased from 10 rpm min⁻¹ to 25 rpm min⁻¹. If the rat fell off the rotarod, it was placed back on until the 300-s training period was completed. During the behavioral test, the speed was set to 25 rpm min⁻¹, and the time each rat remained on it was recorded over three attempts. If a rat clung to the rotarod and rotated twice, it was

also considered a fall. The maximum time on rod is 300 s, with longer times indicating better motor function. The EBST evaluated asymmetrical motor behavior. The rat is lifted by its tail about 10 cm above the table surface, and the rat exhibits side-to-side swings. If no swing behavior is observed for more than 5 s, gentle tail pinching was used to induce swinging. Each time the rat's head deviated more than 10° from the vertical axis to one side, it was recorded as a swing. Each rat underwent 20 trials, with at least 1-min intervals between trials. The number of swings to the left and right were recorded. Normal rats typically exhibit a right-side swing ratio of approximately 0.5 in the EBST, whereas stroke rats, due to left-sided brain injury, display a rightward bias, resulting in a ratio exceeding 0.5. The closer the right-side swing ratio is to 0.5 in the EBST, the better the recovery of the rat.

Immunological staining of brain sections

In accordance with the experimental design, rats were transcardially perfused with PBS and 4 wt.% PFA on Days 1, 7, 14, and 28 following the injection of therapeutic substance. Following perfusion, brains were carefully extracted and post-fixed in 4 wt.% PFA for 4 h at 4 °C. Subsequently, tissues were dehydrated in 30 wt.% sucrose solution at 4 °C until they fully sank, indicating adequate cryoprotection and minimizing ice crystal formation to preserve cellular morphology and tissue integrity. After dehydration, excess sucrose was gently blotted with absorbent paper, and the brains were embedded in optimal cutting temperature (OCT) compound within embedding molds. Care was taken to eliminate air bubbles around the tissue to ensure uniform embedding. The molds were then placed in a -80 °C freezer until the OCT block solidified completely. Frozen brain samples were sectioned into 25 µm-thick coronal slices using a cryostat (Leica CM1950) for subsequent histological and immunofluorescence analyses. Three to four brain sections spanning the entire injury area were selected from each sample for the subsequent immunostaining procedures. The sections were initially fixed in 4 wt.% PFA for 10 min, followed by permeabilization in 0.3 wt.% Triton ×-100 solution for 10 min. After blocking with 1 wt.% BSA for 1 h. sections were incubated with the following primary antibodies at 4 °C for more than 16 h: rabbit anti-Ki67 (1:200, Abcam), goat anti-CD31 (1:200, R&D), mouse anti-Nestin (1:200, Millipore), rabbit anti-DCX (1:200, Abcam), goat anti-GFAP (1:400, Abcam), rabbit anti-NeuN (1:200, Millipore), mouse anti-APC (1:100, Millipore), and rabbit anti-NG2 (1:100, Millipore). Specific information for the antibodies is listed in the Supplementary Table 1. The sections were subsequently washed three times with PBS and incubated with the appropriate secondary antibodies, including Alexa Fluor 594-conjugated donkey anti-rabbit, donkey anti-goat, and donkey anti-mouse, as well as Alexa Fluor 647-conjugated donkey antirabbit, and additional Alexa Fluor 594-conjugated secondary antibodies as needed. Following incubation with the secondary antibody, the sections were rinsed three times with PBS, with each wash lasting 15 min. Subsequently, the sections were coverslipped using a mounting medium containing DAPI.

For TUNEL staining, the brain sections were processed according to the instructions provided with the One-Step TUNEL Apoptosis Detection Kit (Meilunbio, Shanghai, China). The steps prior to staining were similar to immunofluorescence staining, but the TdT enzyme and fluorescent labeling solution were mixed at a ratio of 1:9 as the diluent for the secondary antibody. The sections were washed three times with PBS and then mounted.

For image acquisition, high-resolution images were obtained using a confocal laser scanning microscope (FV3000), while large-field stitched images were acquired with a fluorescence upright microscope (Leica). For fluorescence quantification, 3–4 rats were included in each experimental group. Three to four brain sections were obtained from each rat, and three to four random fields per section were imaged in the peri-infarct or infarct core region and subjected to statistical analysis. Positive cells were manually counted using LAS AF Lite software.

IOD of vessels was measured using ImageJ, following background subtraction and thresholding to ensure accurate detection of vascular structures. Data were then analyzed using Prism GraphPad 9 (GraphPad Software, San Diego, USA).

Vascular evaluations of brain sections

The quantification of junction numbers and vessel diameters were conducted using AngioTool (2.0), a specialized software designed for the analysis of vascular networks. All 2D images of CD31 immunostaining were stored in a single folder and processed using a batch module. The fluorescence threshold of the images was adjusted to optimize the vascular network and obtain the output images, where the red regions represent the identified vessel skeletons and the blue dots indicate the connection points between vessels. Finally, the junction numbers were counted with the connection points between vessels.

Cresyl violet staining of rat brain slices

To assess tissue morphology and quantify brain atrophy, Cresyl Violet staining was performed on brain sections collected 28 days posttransplantation. Following cryosectioning, brain sections were airdried completely to ensure dehydration. The sections were then stained with a 0.1 wt.% Cresyl Violet solution (Sigma-Aldrich) at room temperature for 3-10 min. Staining intensity was evaluated under a microscope to check the staining duration until optimal intensity was achieved. If overstaining occurred, sections were briefly differentiated in 95% ethanol for 1–5 s to obtain optimal contrast. Subsequently, the sections were thoroughly rinsed by repeated immersion in distilled water to remove excess dye, followed by a 30-min rinse under running water to eliminate residual stain. The sections were then air-dried and scanned directly. For quantification, the area of the ipsilateral and contralateral hemisphere was measured by Imagel software. The height (H) represented the spacing between two neighboring brain slices, with the atrophy areas of these paired slices designated as ΔS_n and ΔS_{n+1} . The overall brain atrophy volume was then calculated based on the following formula:

$$V = \sum \frac{H}{3} \times \left[\Delta S_n + \sqrt[2]{\Delta S_n \times \Delta S_{n+1}} + \Delta S_{n+1} \right] \tag{1}$$

Statistical analysis

The experimental data were statistically analyzed using GraphPad or Origin software. All data are expressed as means ± SDs. Each point in the bar graphs represents a technically independent sample or a single rat, with n indicating the number of samples or rats. The normality of all datasets was assessed using the Shapiro–Wilk test, which is appropriate for small sample sizes in IBM SPSS Statistics software. Parametric tests were performed on data that followed a normal distribution. Differences among multiple normally distributed groups were analyzed using one-way or multi-way ANOVA, followed by Dunnett's or Tukey's multiple comparisons. For non-normally distributed data, non-parametric tests were applied. Statistical significance is indicated as *p*-values in the graphs.

Ethical approval

All animal experiment procedures in this study were conducted in accordance with ethical guidelines and received approval from the Institutional Animal Care and Use Committee (IACUC) of Shanghai Jiao Tong University, with the animal ethics protocol number 2023006. The experiments in this study adhered to the "Animal Research: Reporting in Vivo Experiments (ARRIVE)" guidelines.

Reporting summary

Further information on research design is available in the Nature Portfolio Reporting Summary linked to this article.

Data availability

All data necessary to support the conclusions of this study are provided in the main text, including the main figures and Supplementary Information. Source data are provided as a Source Data file. Source data are provided with this paper.

References

- Thayabaranathan, T. et al. Global stroke statistics 2022. Int. J. Stroke 17, 946–956 (2022).
- Mendelson, S. J. & Prabhakaran, S. Diagnosis and management of transient ischemic attack and acute ischemic stroke: a review. *JAMA* 325, 1088–1098 (2021).
- Hasan, T. F. et al. Endovascular thrombectomy for acute ischemic stroke. Curr. Cardiol. Rep. 21, 1–12 (2019).
- Rust, R. et al. Brain repair mechanisms after cell therapy for stroke. Brain 147, 3286–3305 (2024).
- Zhang, G. L., Zhu, Z. H. & Wang, Y. Z. Neural stem cell transplantation therapy for brain ischemic stroke: Review and perspectives. World J. Stem Cells 11, 817–830 (2019).
- Kawabori, M., Shichinohe, H., Kuroda, S. & Houkin, K. Clinical trials of stem cell therapy for cerebral ischemic stroke. *Int. J. Mol. Sci.* 21, 7380 (2020).
- Chan, H. H., Wathen, C. A., Ni, M. & Zhuo, S. M. Stem cell therapies for ischemic stroke: current animal models, clinical trials and biomaterials. Rsc Adv. 7, 18668–18680 (2017).
- 8. Bang, O. Y. Clinical trials of adult stem cell therapy in patients with ischemic stroke. *J. Clin. Neurol.* **12**, 14–20 (2016).
- 9. Ejma, M. et al. The role of stem cells in the therapy of stroke. *Curr. Neuropharmacol.* **20**, 630–647 (2022).
- Zhao, T. et al. Neural stem cells therapy for ischemic stroke: progress and challenges. *Transl. Stroke Res.* 13, 665–675 (2022).
- Jiao, Y., Liu, Y. W., Chen, W. G. & Liu, J. Neuroregeneration and functional recovery after stroke: advancing neural stem cell therapy toward clinical application. *Neural Regen. Res.* 16, 80–92 (2021).
- Tapeinos, C. et al. Advanced functional materials and cell-based therapies for the treatment of ischemic stroke and postischemic stroke effects. Adv. Funct. Mater. 30, 1906283 (2020).
- Lam, J., Lowry, W. E., Carmichael, S. T. & Segura, T. Delivery of iPS-NPCs to the stroke cavity within a hyaluronic acid matrix promotes the differentiation of transplanted cells. Adv. Funct. Mater. 24, 7053–7062 (2014).
- Zweckberger, K., Ahuja, C. S., Liu, Y., Wang, J. & Fehlings, M. G. Selfassembling peptides optimize the post-traumatic milieu and synergistically enhance the effects of neural stem cell therapy after cervical spinal cord injury. Acta Biomater. 42, 77–89 (2016).
- Bible, E. et al. The support of neural stem cells transplanted into stroke-induced brain cavities by PLGA particles. *Biomaterials* 30, 2985–2994 (2009).
- George, P. M. et al. Electrical preconditioning of stem cells with a conductive polymer scaffold enhances stroke recovery. *Biomaterials* 142, 31–40 (2017).
- Daly, A. C., Riley, L., Segura, T. & Burdick, J. A. Hydrogel microparticles for biomedical applications. *Nat. Rev. Mater.* 5, 20–43 (2020).
- Caldwell, A. S., Aguado, B. A. & Anseth, K. S. Designing microgels for cell culture and controlled assembly of tissue microenvironments. Adv. Funct. Mater. 30, 1907670 (2020).
- Caprio, N. D., Davidson, M. D., Daly, A. C. & Burdick, J. A. Injectable MSC spheroid and microgel granular composites for engineering tissue. Adv. Mater. 36, e2312226 (2024).
- Griffin, D. R., Weaver, W. M., Scumpia, P. O., Di Carlo, D. & Segura, T. Accelerated wound healing by injectable microporous gel scaffolds assembled from annealed building blocks. *Nat. Mater.* 14, 737–744 (2015).

- Sideris, E. et al. Particle hydrogels decrease cerebral atrophy and attenuate astrocyte and microglia/macrophage reactivity after stroke. Adv. Ther. (Weinh) 5, 2200048 (2022).
- Morley, C. D., Ding, E. A., Carvalho, E. M. & Kumar, S. A Balance between inter- and intra-microgel mechanics governs stem cell viability in injectable dynamic granular hydrogels. *Adv. Mater.* 35, e2304212 (2023).
- Thomas, D. et al. Temporal changes guided by mesenchymal stem cells on a 3D microgel platform enhance angiogenesis in vivo at a low-cell dose. *Proc. Natl. Acad. Sci. USA* 117, 19033–19044 (2020).
- Sun, J. et al. Mesenchymal stem cell-laden composite β cell porous microgel for diabetes treatment. Adv. Funct. Mater. 33, 2211897 (2023).
- Wang, M. et al. A multifunctional micropore-forming bioink with enhanced anti-bacterial and anti-inflammatory properties. *Biofab*rication 14, 024105 (2022).
- Qin, X. S., Wang, M. A., Li, W. L. & Zhang, Y. S. Biosurfactantstabilized micropore-forming GelMA inks enable improved usability for 3D printing applications. *Regen. Eng. Transl. Med.* 8, 471–481 (2022).
- 27. Wang, M. et al. Digital light processing based bioprinting with composable gradients. *Adv. Mater.* **34**, e2107038 (2022).
- Lee, K. Y. & Mooney, D. J. Alginate: properties and biomedical applications. Prog. Polym. Sci. 37, 106–126 (2012).
- Alesso, M., Bondioli, G., Talío, M. C., Luconi, M. O. & Fernández, L. P. Micelles mediated separation fluorimetric methodology for Rhodamine B determination in condiments, snacks and candies. Food Chem. 134, 513–517 (2012).
- Qazi, T. H., Muir, V. G. & Burdick, J. A. Methods to characterize granular hydrogel rheological properties, porosity, and cell invasion. ACS Biomater. Sci. Eng. 8, 1427–1442 (2022).
- Muir, V. G. et al. Influence of microgel and interstitial matrix compositions on granular hydrogel composite properties. Adv. Sci. 10, 2206117 (2023).
- Takahashi, R. et al. Tough particle-based double network hydrogels for functional solid surface coatings. Adv. Mater. Interfaces 5, 1801018 (2018).
- Wyss, C. S., Karami, P., Demongeot, A., Bourban, P. E. & Pioletti, D. P. Silk granular hydrogels self-reinforced with regenerated silk fibroin fibers. Soft Matter 17, 7038–7046 (2021).
- 34. Suchting, S. & Eichmann, A. Jagged gives endothelial tip cells an edge. Cell 137, 988–990 (2009).
- Caplan, A. I. All MSCs are pericytes?. Cell Stem Cell 3, 229–230 (2008).
- Qazi, T. H. et al. Anisotropic rod-shaped particles influence injectable granular hydrogel properties and cell invasion. Adv. Mater. 34, e2109194 (2022).
- Doeppner, T. R. et al. Effects of acute versus post-acute systemic delivery of neural progenitor cells on neurological recovery and brain remodeling after focal cerebral ischemia in mice. Cell Death Dis. 5, e1386 (2014).
- Nih, L. R., Gojgini, S., Carmichael, S. T. & Segura, T. Dual-function injectable angiogenic biomaterial for the repair of brain tissue following stroke. *Nat. Mater.* 17, 642 (2018).
- Reeson, P. et al. Delayed inhibition of VEGF signaling after stroke attenuates blood-brain barrier breakdown and improves functional recovery in a comorbidity-dependent manner. J. Neurosci. 35, 5128–5143 (2015).
- Krupinski, J. et al. Three-dimensional structure and survival of newly formed blood vessels after focal cerebral ischemia. Neuroreport 14, 1171–1176 (2003).
- Lei, Y. et al. Stem cell-recruiting injectable microgels for repairing osteoarthritis. Adv. Funct. Mater. 31, 2105084 (2021).

- Nih, L. R., Carmichael, S. T. & Segura, T. Hydrogels for brain repair after stroke: an emerging treatment option. *Curr. Opin. Biotechnol.* 40, 155–163 (2016).
- 43. Hatakeyama, M., Ninomiya, I. & Kanazawa, M. Angiogenesis and neuronal remodeling after ischemic stroke. *Neural Regen. Res.* **15**, 16–19 (2020).
- 44. Paro, M. R. et al. Molecular mediators of angiogenesis and neurogenesis after ischemic stroke. *Rev. Neurosci.* **34**, 425–442 (2023).
- Li, Y., Song, W., Kong, L., He, Y. & Li, H. Injectable and microporous microgel-fiber granular hydrogel loaded with bioglass and siRNA for promoting diabetic wound healing. Small 20, e2309599 (2024).
- Wu, S. et al. An injectable multicomponent integrated microgel promotes cardiomyocyte regeneration and heart function after ischemia reperfusion injury. Chem. Eng. J. 498, 155137 (2024).
- Williamson, M. R., Fuertes, C. J. A., Dunn, A. K., Drew, M. R. & Jones, T. A. Reactive astrocytes facilitate vascular repair and remodeling after stroke. *Cell Rep.* 35, 109048 (2021).
- 48. Barsanti, S. et al. Structural analysis of astrocytes in different experimental conditions. *Glia* **71**, E509–E509 (2023).
- Fernando, I. P. S., Lee, W., Han, E. J. & Ahn, G. Alginate-based nanomaterials: fabrication techniques, properties, and applications. Chem. Eng. J. 391, 123823 (2020).
- Xu, M. J. et al. Alginate microgels as delivery vehicles for cell-based therapies in tissue engineering and regenerative medicine. *Carbohyd. Polym.* 266, 118128 (2021).
- Aisenbrey, E. A. & Murphy, W. L. Synthetic alternatives to Matrigel. Nat. Rev. Mater. 5, 539–551 (2020).
- Tang, G. et al. Gas-Shearing fabrication of multicompartmental microspheres: a one-step and oil-free approach. Adv. Sci. (Weinh.)
 1802342 (2019).
- Tang, G. S. et al. Designable dual-power micromotors fabricated from a biocompatible gas-shearing strategy. *Chem. Eng. J.* 407, 127187 (2021).
- 54. Zhu, Z. et al. Free-boundary microfluidic platform for advanced materials manufacturing and applications. *Adv. Mater.* **36**, e2304840 (2024).
- 55. Li, X.-B. et al. Study on the mechanism of droplet formation in T-junction microchannel. *Chem. Eng. Sci.* **69**, 340–351 (2012).
- van de Velde, F., Weinbreck, F., Edelman, M. W., van der Linden, E. & Tromp, R. H. Visualisation of biopolymer mixtures using confocal scanning laser microscopy (CSLM) and covalent labelling techniques. *Colloids Surf. B: Biointerfaces* 31, 159–168 (2003).
- Fischer, E. R., Hansen, B. T., Nair, V., Hoyt, F. H. & Dorward, D. W. Scanning electron microscopy. *Curr. Protoc. Microbiol.* 25, 2B (2012).
- Highley, C. B., Song, K. H., Daly, A. C. & Burdick, J. A. Jammed microgel inks for 3D printing applications. Adv. Sci. (Weinh.) 6, 1801076 (2019).
- 59. van Duinen, V. et al. Perfused 3D angiogenic sprouting in a high-throughput in vitro platform. *Angiogenesis* **22**, 157–165 (2019).
- 60. Song, K. H., Highley, C. B., Rouff, A. & Burdick, J. A. Complex 3D-printed microchannels within cell-degradable hydrogels. *Adv. Funct. Mater.* **28**, 1801331 (2018).

Acknowledgements

This work was supported by the National Key Research and Development Program of China (2023YFA1801803, 2022YFA1105103 to M.W.), the National Natural Science Foundation of China (32371474 to M.W., 32301146 to W.L., 32330030 to S.G., 92168205 to S.G., 81901894 to M.W.), the Shanghai Science and Technology PuJiang Funds 09PJ1401500 to M.W., Shanghai Sailing Program 23YF1420700 to W.L., the Fundamental Research Funds for the Central Universities 22120240435 to S.G., Peak Disciplines (Type IV) of Institutions of Higher Learning in Shanghai.

Author contributions

M.W., W.L., and S.G. conceived the research and wrote the manuscript. H.W., Z.L. (Ze Liu), Z.Z., Z.L. (Zhongqing Liu), Z.G., M.M., H.L., Y.L., and S.W. performed the experiments and analyzed the experimental results. M.W., W.L., S.G., G.T., and G.Y.Y. supervised the study. All authors commented on and/or edited the manuscript.

Competing interests

The authors declare no competing interests.

Additional information

Supplementary information The online version contains supplementary material available at https://doi.org/10.1038/s41467-025-64240-1.

Correspondence and requests for materials should be addressed to Wanlu Li, Shaorong Gao or Mian Wang.

Peer review information *Nature Communications* thanks Tatiana Segura, who co-reviewed with Andrea Jones and Cara Smith, and the other, anonymous, reviewer for their contribution to the peer review of this work. A peer review file is available.

Reprints and permissions information is available at

http://www.nature.com/reprints

Publisher's note Springer Nature remains neutral with regard to jurisdictional claims in published maps and institutional affiliations.

Open Access This article is licensed under a Creative Commons Attribution-NonCommercial-NoDerivatives 4.0 International License, which permits any non-commercial use, sharing, distribution and reproduction in any medium or format, as long as you give appropriate credit to the original author(s) and the source, provide a link to the Creative Commons licence, and indicate if you modified the licensed material. You do not have permission under this licence to share adapted material derived from this article or parts of it. The images or other third party material in this article are included in the article's Creative Commons licence, unless indicated otherwise in a credit line to the material. If material is not included in the article's Creative Commons licence and your intended use is not permitted by statutory regulation or exceeds the permitted use, you will need to obtain permission directly from the copyright holder. To view a copy of this licence, visit http://creativecommons.org/licenses/by-nc-nd/4.0/.

© The Author(s) 2025